Supplementary Information

S1 Weather station networks

We used air data from ten automatic weather stations (AWSs) in the Khumbu and Langtang regions of Nepal to characterise the 4 October 2025 event (Fig. S1 and Table S1). Importantly, we highlight that the precipitation measurements at EBC—the focus of our assessment—were made with a high-quality, weighing (OTT Pluvio^2) gauge, protected by a double Alter shield (Matthews et al., 2020), and are therefore considered to be very reliable. Although precipitation measurements are available from Pyramid, we do not use them here because close inspection indicates that they were unreliable during the 4 October 2025 event, most likely owing to capping of the gauge by the exceptional snowfall. Two observations support this interpretation. First, the gauge recorded only 24.3 mm l.e. on 4 October, substantially less than expected for the event, consistent with snow being prevented from entering the bucket. Second, an unphysical accumulation of 36 mm l.e. was recorded in just 30 minutes on the morning of 5 October. The latter is consistent with displacement of the snow cap, plausibly triggered by the rapid rise in air temperature at that time (Fig. 1 in main text).

S2 Physical controls on temperature evolution

In the main text, we discuss controls on the development of an isothermal near 0 °C layer formed by the melting of precipitating frozen hydrometeors. Here, we provide further context. We begin by noting that the Eulerian pressure-coordinate enthalpy budget for an atmospheric layer bounded by pressure surfaces $p_b$and $p_t$can be written approximately as:

$$\frac{\partial}{\partial t}\left[\frac{1}{g}\int_{pt}^{pb} c_p\, T\, dp\right] = \frac{1}{g}\int_{p_t}^{p_b} -\mathbf{u}\cdot\nabla_{\boldsymbol{p}}\,(c_pT) - c_p\,\omega\left(\frac{T}{\theta}\frac{\partial\theta}{\partial p}\right) + \dot{d}\, dp \qquad \text{(S1)}$$

where $\mathbf{u}$ is the horizontal wind vector, $\nabla_{\boldsymbol{p}}$ is the horizontal gradient on a constant-pressure surface, ω is the vertical velocity in pressure coordinates, θ is potential temperature, c_p is the specific heat capacity at constant pressure, and $\dot{d}$ is the diabatic heating rate per unit mass. The first and second terms therefore represent horizontal temperature advection and vertical motion tendency, respectively; the third term represents diabatic heating or cooling. In a saturated air parcel, the major controls on $\dot{d}$ can be approximated by:

$$\dot{d} = L_v C - L_f M \qquad \text{(S2)}$$

where C and M are, respectively, the condensation and melting rates per unit mass of air; and L_v and L_f are, respectively, the enthalpies of vaporisation and fusion. The first term on the right-hand-side of Eq. (S2) is therefore the condensational heating, and the second term represents cooling from melting hydrometeors, which depends on the precipitation rate (P). This rate is, in turn, related to the net condensation occurring throughout the depth of the atmosphere above p_t, which (all else equal) scales with the vertical velocity (ω) and the gradient in the saturation specific humidity (q_s):

$$P \simeq \frac{1}{g}\int_{p_u}^{p_t} C\ dp \simeq -\frac{1}{g}\int_{p_u}^{p_t} \omega\frac{dq_s}{d_p}\ dp \qquad \text{(S3)}$$

where, p_u is the pressure at the upper boundary of the atmospheric column. Note that whilst Eq. (S3) is a simple scaling relation, its form helps illuminate the first-order controls on P. First, ω in mountainous terrain depends strongly on the horizontal wind vector ($\mathbf{u}$) and the terrain slope vector (∇z_s), so Eq. (S3) can be approximated as Roe (2005):

$$P \simeq \frac{1}{g}\int_{p_u}^{p_t} \rho\, g\, (\mathbf{u}\cdot\nabla z_s)\, \frac{dq_s}{d_p}\, dp \qquad \text{(S4)}$$

The integrated latent heating associated with condensation throughout the atmospheric column will typically far exceed cooling associated with melting because the latent heat of vaporization (L_v) is almost an order of magnitude larger than the latent heat of fusion (L_f). However, condensation and melting occur in different parts of the atmosphere. Whereas condensational heating is distributed over a deep atmospheric layer, cooling from melting is concentrated locally where frozen hydrometeors encounter regions of positive T, allowing local melt-induced cooling to exceed local condensational warming (Kain et al., 2000).

Equations (S1)–(S4) show how melting can create and maintain a 0 °C isothermal layer. Snow falling through air at temperatures above 0 °C begins to melt, producing a cooling tendency whose magnitude depends on the precipitation intensity (equations (S2)–(S4)). Where this diabatic cooling outweighs the combined warming tendencies in Eq. (S1), the net temperature tendency is negative and the air cools towards 0 °C. Once 0 °C is reached, a quasi-steady isothermal layer can develop where melting-induced cooling approximately balances the other temperature tendencies, with continued heat input consumed by further melting rather than appreciably warming the air. The layer may then propagate downward into warmer air for as long as the supply of falling snow and the associated latent-heat sink are sufficient to cool newly encountered air to 0 °C.

The pressure thickness of air (Δp) that can be cooled to 0 °C depends on the balance between the melt-induced energy sink and the sensible heat that must be removed from the layer. If a mass of precipitation (ΔP) melts within a layer whose mass-weighted temperature excess above 0 °C is $\bar{T}$, then:

$$C_p \left(\frac{\Delta p}{g}\right) \bar{T} \;\simeq L_f \Delta P \qquad \text{(S5)}$$

and, therefore:

$$\Delta p \simeq \frac{\mathrm{g}\, L_f \Delta P}{C_p\, \bar{T}} \qquad \text{(S6)}$$

Equations (S5) and (S6) neglect the other advective and diabatic terms in Eq. (S1); they therefore provide an upper estimate of Δp if the omitted terms are assumed to cause net warming. Applying Eq. (6) here illustrates that the precipitation intensity was more than sufficient to produce the observed 0 °C isothermal layer. The mass-weighted mean temperature excess above 0 °C ($\bar{T}$) for the reference temperature profile (red line in Fig. S5) between 565 and 609 hPa—the mean barometric pressures at the top and bottom of the isothermal layer, respectively—was 2.6 °C. Using, for illustration, the 4.9 mm of precipitation that accumulated between 04:00 and 05:00 on 4 October 2025 (corresponding to the hour during which the largest drop in the 0 °C isotherm occurred: Fig. 1 in the main paper), Eq. (S6) indicates that this precipitation would have produced an isothermal layer with a thickness (Δp) of ~62 hPa, exceeding the observed thickness of 44 hPa.

Taken together, the ingredients for deep isothermal layers (large Δp) are now clear. Favourable conditions include high precipitation rates (equations (S5) and (S6)), encouraged by strong winds aloft impinging on steep terrain (Eq. (S4)), together with weak compensating advective and condensational heating terms within the region of layer formation (Eq. (S1)). The deep Khumbu Valley, flanked by very steep mountain sides, appears to possess several characteristics conducive to large Δp that can reach the surface at glacierised elevations. It is an environment of strong vertical wind shear (Matthews et al., 2020) that can support intense precipitation through high winds aloft and orographic ascent, whilst near-surface advective tendencies may remain relatively weak within the sheltered valleys, where flow can become partially decoupled from the atmosphere aloft (Schauwecker et al., 2022). Such decoupling may be further enhanced if diabatic cooling from melting hydrometeors increases static stability, thereby suppressing vertical mixing with air aloft. Near-surface temperatures within these steep, glacierised valleys at the onset of extreme precipitation events are also typically close to the melting point (Kain et al., 2000; Perry et al., 2020) and, therefore, to the temperatures at which potential snowfall intensities are maximised (O'Gorman, 2014). Additionally, extreme precipitation occurring upwind can reduce downstream warm advection because arriving air masses have already undergone substantial diabatic cooling. The extreme precipitation observed at Langtang, west of the Khumbu Valley, is consistent with this mechanism. Temperature observations also offer support, with cooler conditions at comparable elevations in the Khumbu region (Fig. 1 main text and Fig. S3), suggesting cumulative diabatic cooling from melting hydrometeors as the storm progressed downwind (Marwitz, 1987).

In the main paper, we illustrate the potential impact of background warming on the evolution of the 0 °C isothermal layer if Δp remains unchanged. This warming experiment should therefore be interpreted as a conditional geometric sensitivity, not a full assessment of the potential future melt-layer response. We prescribe Δp to ask how a similar pressure-thickness isothermal layer would map into height coordinates as the ambient 0 °C level rises. In reality, Δp depends on the full Eq. (S1) balance, including precipitation intensity, condensational heating, horizontal and vertical advective tendencies. All these terms might be sensitive to large-scale warming.

Supplementary References

Eeckman, J., Chevallier, P., Boone, A., Neppel, L., De Rouw, A., Delclaux, F., and Koirala, D.: Providing a non-deterministic representation of spatial variability of precipitation in the Everest region, Hydrology and Earth System Sciences, 21, 4879–4893, https://doi.org/10.5194/hess-21-4879-2017, 2017.

Graves, B., Matthews, T., Perry, L. B., Edwards, T., Taylor, R., Brun, F., Wagnon, P., Khadka, A., and Shrestha, D.: Modelling accumulation of a high-altitude Himalayan glacier, Journal of Glaciology, 72, e32, https://doi.org/10.1017/jog.2026.10147, 2026.

ICIMOD: River Network of Hindu Kush Himalayan (HKH) Region, http://rds.icimod.org:8080/geonetwork/srv/api/records/7b703c27-f6b2-4803-8fdc-669694428c69, 2007.

Kain, J. S., Goss, S. M., and Baldwin, M. E.: The Melting Effect as a Factor in Precipitation-Type Forecasting, Weather and Forecasting, 15, 700–714, https://doi.org/10.1175/1520-0434(2000)015%3C0700:TMEAAF%3E2.0.CO;2, 2000.

Khadka, A., Wagnon, P., Brun, F., Shrestha, D., Lejeune, Y., and Arnaud, Y.: Evaluation of ERA5-Land and HARv2 Reanalysis Data at High Elevation in the Upper Dudh Koshi Basin (Everest Region, Nepal), Journal of Applied Meteorology and Climatology, 61, 931–954, https://doi.org/10.1175/JAMC-D-21-0091.1, 2022.

Marwitz, J. D.: Deep Orographic Storms over the Sierra Nevada. Part I: Thermodynamic and Kinematic Structure, Journal of the Atmospheric Sciences, 44, 159–173, https://doi.org/10.1175/1520-0469(1987)044%3C0159:DOSOTS%3E2.0.CO;2, 1987.

Matthews, T., Perry, L. B., Koch, I., Aryal, D., Khadka, A., Shrestha, D., Abernathy, K., Elmore, A. C., Seimon, A., Tait, A., Elvin, S., Tuladhar, S., Baidya, S. K., Potocki, M., Birkel, S. D., Kang, S., Sherpa, T. C., Gajurel, A., and Mayewski, P. A.: Going to Extremes: Installing the World's Highest Weather Stations on Mount Everest, Bull. Amer. Meteor. Soc., https://doi.org/10.1175/BAMS-D-19-0198.1, 2020.

Mimeau, L., Esteves, M., Jacobi, H.-W., and Zin, I.: Evaluation of Gridded and In Situ Precipitation Datasets on Modeled Glacio-Hydrologic Response of a Small Glacierized Himalayan Catchment, Journal of Hydrometeorology, 20, 1103–1121, https://doi.org/10.1175/JHM-D-18-0157.1, 2019.

NASA/METI/AIST/Japan Spacesystems and U.S./Japan ASTER Science Team: ASTER Global Digital Elevation Model V003, https://doi.org/10.5067/ASTER/ASTGTM.003, 2019.

O'Gorman, P. A.: Contrasting responses of mean and extreme snowfall to climate change, Nature, 512, 416–418, https://doi.org/10.1038/nature13625, 2014.

Paulhus, J. L. H.: RECORD SNOWFALL OF APRIL 14–15, 1921, AT SILVER LAKE, COLORADO, Monthly Weather Review, 81, 38–40, https://doi.org/10.1175/1520-0493(1953)081%3C0038:RSOAAS%3E2.0.CO;2, 1953.

Perry, L. B., Matthews, T., Guy, H., Koch, I., Khadka, A., Elmore, A. C., Shrestha, D., Tuladhar, S., Baidya, S. K., Maharjan, S., Wagnon, P., Aryal, D., Seimon, A., Gajurel, A., and Mayewski, P. A.: Precipitation Characteristics and Moisture Source Regions on Mt. Everest in the Khumbu, Nepal, One Earth, 3, 594–607, https://doi.org/10.1016/j.oneear.2020.10.011, 2020.

RGI 7.0 Consortium: Randolph Glacier Inventory - A Dataset of Global Glacier Outlines, Version 7.0, https://doi.org/doi:10.5067/f6jmovy5navz, 2023.

Roe, G. H.: OROGRAPHIC PRECIPITATION, Annual Review of Earth and Planetary Sciences, 33, 645–671, https://doi.org/10.1146/annurev.earth.33.092203.122541, 2005.

Schauwecker, S., Palma, G., MacDonell, S., Ayala, Á., and Viale, M.: The Snowline and 0°C Isotherm Altitudes During Precipitation Events in the Dry Subtropical Chilean Andes as Seen by Citizen Science, Surface Stations, and ERA5 Reanalysis Data, Front. Earth Sci., 10, https://doi.org/10.3389/feart.2022.875795, 2022.

Steiner, J. F., Gurung, T. R., Joshi, S. P., Koch, I., Saloranta, T., Shea, J., Shrestha, A. B., Stigter, E., and Immerzeel, W. W.: Multi-year observations of the high mountain water cycle in the Langtang catchment, Central Himalaya, Hydrological Processes, 35, e14189, https://doi.org/10.1002/hyp.14189, 2021.

Veals, P. G., Pletcher, M., Schwartz, A. J., Chase, R. J., Harnos, K., Correia, J., Wessler, M. E., and Steenburgh, W. J.: Predicting Snow-to-Liquid Ratio in the Mountains of the Western United States, Weather and Forecasting, 40, 1825–1838, https://doi.org/10.1175/WAF-D-24-0233.1, 2025.

Wasserstein, M. L. and Steenburgh, W. J.: Diverse Characteristics of Extreme Orographic Snowfall Events in Little Cottonwood Canyon, Utah, Monthly Weather Review, 152, 945–966, https://doi.org/10.1175/MWR-D-23-0206.1, 2024.

Supplementary Tables

Table S1: Automatic weather station (AWS) used in this study. Variables are abbreviated as follows: T is air temperature; RH is relative humidity; P is precipitation; p is barometric air pressure; and WS is wind speed. References provide full details about the sensor arrays. *Note that the tipping bucket described in Eeckman et al. (2017) was replaced by a Precis Mecanique tipping bucket in November 2023. †Panch Pokhari measurements are unpublished and provided here: T and Pr were obtained from an ATMOS 41 all-in-one weather station (METER Group).

Station name (abbreviation)	**Region**	**Lat (°)**	**Lon (°)**	**Elevation (m asl)**	**Variables used in this study**	**Reference**
Camp II	Khumbu	27.98	86.90	6464	T, p	(Matthews et al., 2020)
Everest Base Camp (EBC)	Khumbu	28.00	86.84	5315	T, RH, P, WS	(Matthews et al., 2020)
Phortse	Khumbu	27.84	86.74	3810	T, RH, P, WS	(Matthews et al., 2020)
Pyramid	Khumbu	27.96	86.81	5035	T	(Khadka et al., 2022)
Khare	Khumbu	27.75	86.87	4888	T	(Khadka et al., 2022)
Pheriche	Khumbu	27.90	86.82	4260	T, P, WS	(Khadka et al., 2022)
Pangboche	Khumbu	27.86	86.79	3952	T	(Mimeau et al., 2019)
*Phakding	Khumbu	27.74	86.71	2610	T	(Eeckman et al., 2017)
Langshisha	Langtang	28.20	85.69	4452	T, P	(Steiner et al., 2021)
†Panch Pokhari	Langtang	28.04	85.71	4062	T, P	-

Table S2: Extreme liquid equivalent (l.e.) snowfall during the 4 October 2025 event and comparison to other events documented in the literature or available through the U.S. National Oceanic and Atmospheric Administration (NOAA) Automated Surface Observing System (ASOS; identified using precipitation amounts and METAR codes across the full period of data availability for each station). The authors are also aware of some undocumented cases of l.e. increases of >150 mm within 24 hours recorded by snow pillows in the western U.S. and in Chile and Argentina during extreme snowfall events. *Corrected for undercatch following Graves et al. (2026). †Prorated based on 27.5 hr manual measurement.

Event Location (elevation, m asl)	**Precipitation (mm l.e.)**	**Date**	**Source**
12-hr Duration			
Everest Base Camp, Nepal (5,315)	*113.0	4 October 2025	This study
Alta, UT, USA (2,945)	89.7	5 January 2008	(Wasserstein and Steenburgh, 2024)
Blue Canyon, CA, USA (1,611)	76.4	28 February 2023	NOAA ASOS
Stampede Pass, WA, USA (1,210)	59.2	12 January 2021	NOAA ASOS
24-hr Duration			
Everest Base Camp, Nepal (5,315)	*149.0	4 October 2025	This study
Blue Canyon, CA, USA (1,611)	133.1	27-28 February 2023	NOAA ASOS
Silver Lake, CO, USA (3,115)	†124.5	14-15 April 1921	(Paulhus, 1953)
Alta, UT, USA (2,945)	103.4	18-19 December 2010	(Veals et al., 2025)
Stampede Pass, WA, USA (1,210)	68.8	1-2 December 1998	NOAA ASOS

Supplementary Figures

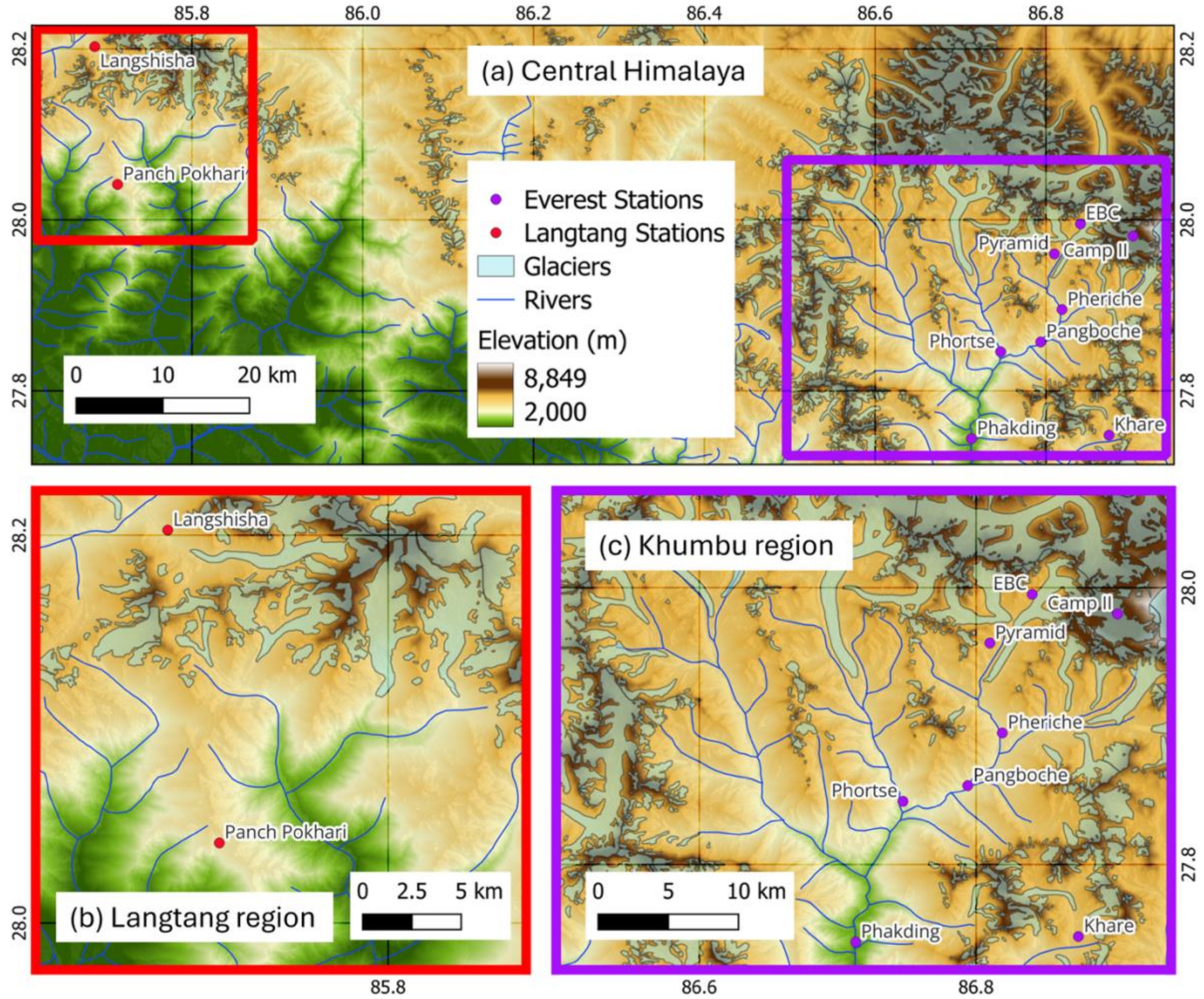

Figure S1: Map indicating the locations of the automatic weather stations (AWSs) used within this analysis (Table S1). Glacier outlines from the Randolph Glacier Inventory (version 7) (RGI 7.0 Consortium, 2023); river outlines are from ICIMOD (ICIMOD, 2007); and the elevation data is ASTER GDEM version 3 (NASA/METI/AIST/Japan Spacesystems and U.S./Japan ASTER Science Team, 2019).'

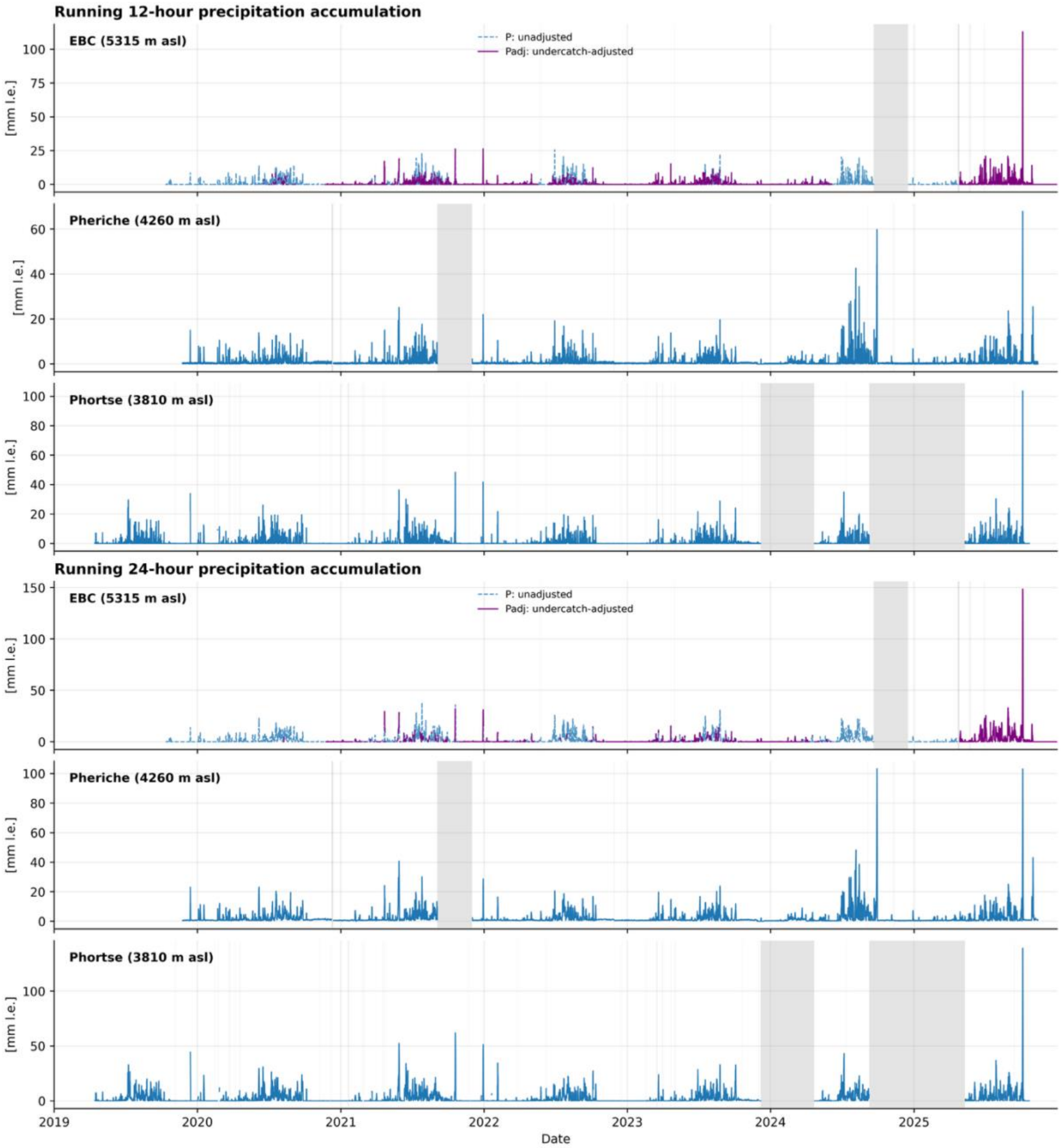

Figure S2: 12- and 24-hour undercatch-corrected precipitation totals at Phortse and Everest Base Camp since installation in 2019. Data from Pheriche during the overlapping period are also provided. Note that, to help contextualise the 4 October 2025 event at EBC, we show raw precipitation for this site when wind speed data (required for the correction) are not available at EBC. Periods of missing data are shown with grey shading.

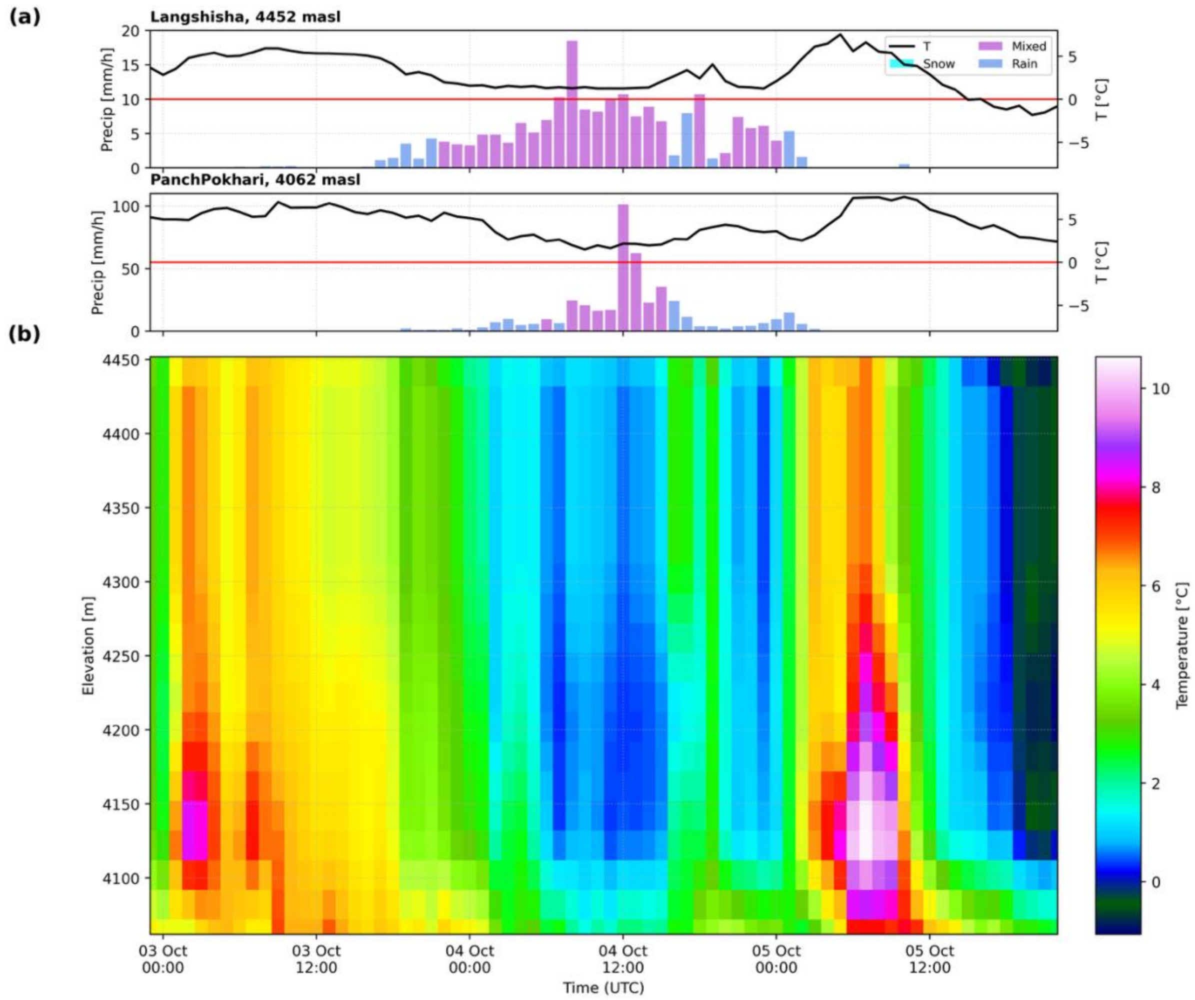

Figure S3: Meteorology at selected weather stations during the 4 October 2025 precipitation event in the Langtang catchment. Time series from automatic weather stations equipped with precipitation sensors are shown in (a). Precipitation phase was classified according to Graves et al. (2026). (b) Elevation-temperature profiles through time for Langtang using temperature data from all stations shown in Table S1.

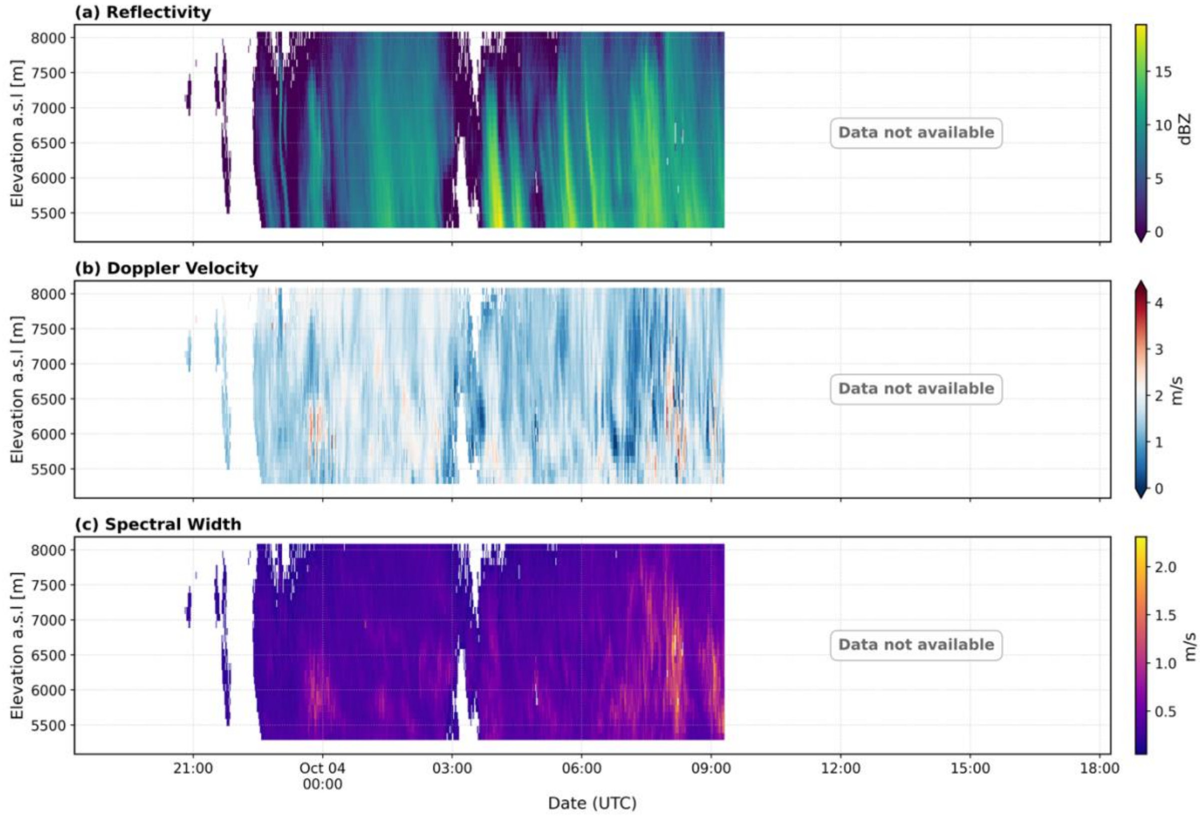

Figure S4: Observations from the Micro Rain Radar (MRR) at Pyramid (5,035 m) showing (a) reflectivity; (b) doppler velocity; and (c) spectral width. Data were not available after 1500 UTC due to a power and/or heater failure at the height of the storm. The MRR time-height profiles indicate a deep precipitating layer extending above 8,000 m asl. There is no discernible melting layer because doppler velocities are consistent with solid precipitation throughout the column. The amplified spectral width (shortly before the instrument lost power) is consistent with increased turbulence.

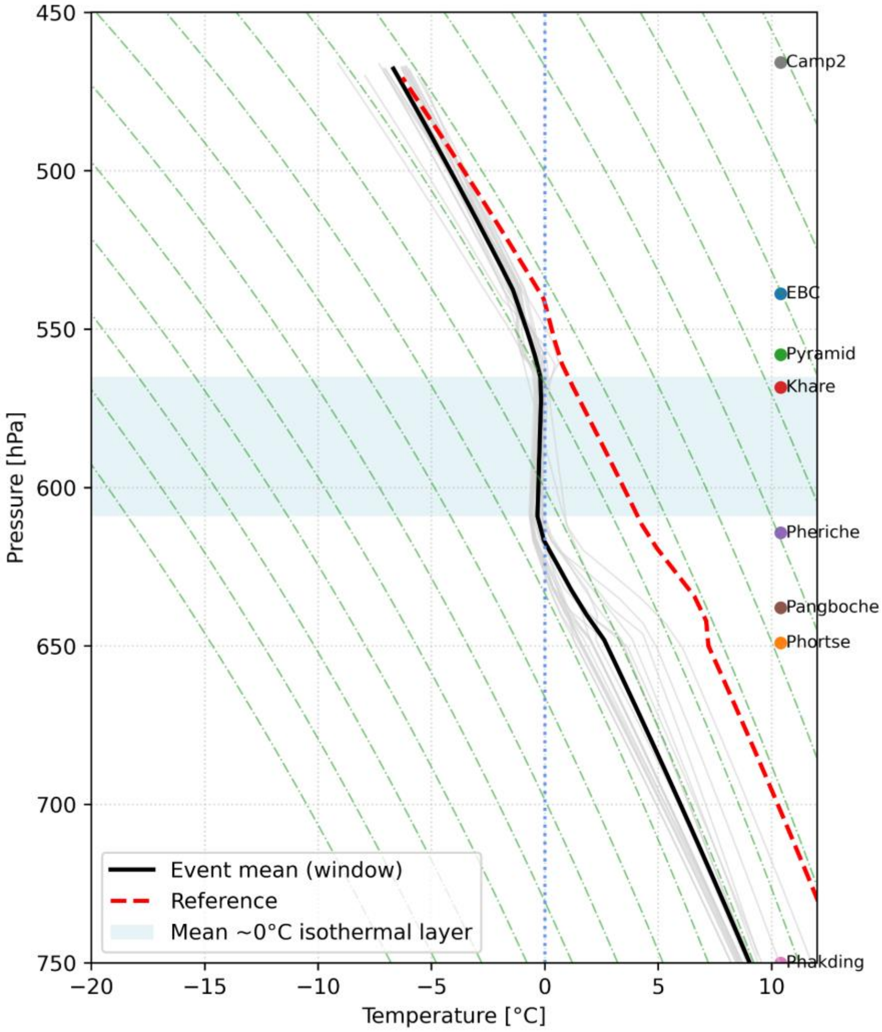

Figure S5: Pressure-temperature profiles during the October snowstorm following the abrupt lowering of the 0 °C isotherm at 04/10/2025 04:00 UTC until 04/10/2025 23:00 UTC. Solid black line is the mean profile, and light-grey lines are the individual hourly profiles. The dashed red 'reference' line is the mean profile for the 24 h ending 03/10/2025 23:00 UTC (shown in Fig. 1 with vertical cyan lines). The light-blue shading marks the ~0 °C isothermal layer according to the mean profile (temperature within 0.5 °C of the melting point, and lapse rate magnitude not exceeding 2°C km^{-1}). The locations of AWSs used to construct temperature profiles are shown as circles.

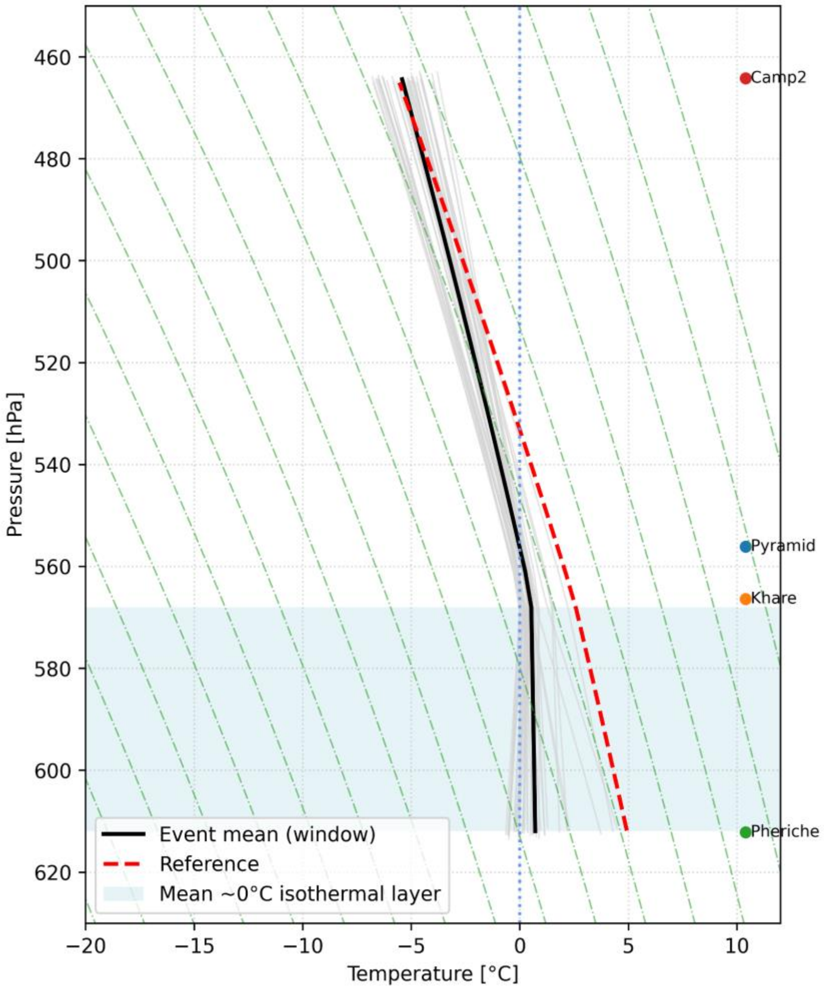

Figure S6: Pressure-temperature profiles for the period 26/09/2024 22:00 UTC-28/09/2024 13:00 UTC– encompassing the second-highest 24 h precipitation total at Pheriche. Solid black line is the mean profile, and light-grey lines are the individual hourly profiles. The dashed red 'reference' line is the mean profile for the 24 h ending 26/09/2024 20:00 UTC. The light-blue shading marks the ~0 °C isothermal layer according to the mean profile, identified following the same method as for Fig. S5. Note that temperature data were available from only a subset of the locations (circles) shown in Fig. S5 during this event.